**Correspondence to:**
D. Tang,
darrell.tang@wur.nl

# Colloid Transport and Retention in Constricted Tube Pore Spaces With Diverse Geometries and Orientations

**Darrell Tang[1]** and **Amir Raoof[2]**

[1]Soil Physics and Land Management, Wageningen University, Wageningen, The Netherlands, [2]Department of Earth Sciences, Utrecht University, Utrecht, The Netherlands

**Abstract** Colloidal contaminants infiltrate and can be attached onto grain surfaces of soils and aquifers, where they may persist. In this study, Lagrangian particle tracking is used to investigate particle trajectories and attachment in pore and fracture spaces modeled as three-dimensional constricted tubes with diverse geometries and orientations relative to gravity. A comprehensive force balance arising from hydrodynamic drag and lift, gravitational settling, Brownian motion, and attractive DLVO interactions is simulated. Results show that the collection efficiency $\eta$ is primarily governed by the dimensionless settling number $S$, representing the relative dominance of gravitational over hydrodynamic forces experienced by the particles. High-$S$ scenarios have larger $\eta$ and are more sensitive to pore orientation, while low-$S$ scenarios are more sensitive to pore geometry. For all scenarios but especially low-$S$ scenarios, the majority of colloid attachment occurs near pore extremities, where fluid velocities are low, such that mechanical remobilization of particles attached is improbable. In low-$S$ scenarios, particles may spread and become immobilized at greater distances from the contamination source owing to lower $\eta$, are harder to mechanically remobilize as they attach more disproportionately at pore extremities, and have trajectories more sensitive to minor forces, rendering their environmental fates complex. Characterizing the collection efficiency and deposition morphology for various pore space geometries and orientations is crucial in understanding particle fate and developing continuum-scale models of colloid transport in real soils, where pore spaces are heterogeneous and advection paths are tortuous.

## 1. Introduction

Soil and groundwater aquifers can become contaminated by the deposition of particulate colloidal pollutants, adversely affecting the subsurface environment (Schmitz, 2006). Particle size determines the dominant processes of colloid retention in porous media (Bradford et al., 2004). Particles with sizes on the order of nanometers have trajectories that are dominated by Brownian motion (Albojamal & Vafai, 2020), and have transport behavior similar to solutes (Seetha et al., 2014). In the environment, such small particles are typically nanoplastics, or viruses and humic substances (McGechan & Lewis, 2002). As particle sizes increase to the micrometer scale, the dominant force becomes the hydrodynamic force (Li et al., 2005), or the gravitational force, depending on the fluid velocity and various other factors. Experimental evidence has shown that the deposition of colloidal particles of diameters on the order of around 1 μm in porous media may be highly dependent on gravitational forces (G. Chen et al., 2010; Ma et al., 2011), especially if the particles are dense (Chrysikopoulos & Syngouna, 2014). Colloidal contaminants in this size range include synthetic microplastics (Khan et al., 2017), bacteria (0.5–3 μm), and clay, mineral, microplastic, or organic particles of diameter 0.1–10 μm (McGechan & Lewis, 2002). For millimeter scale and larger colloidal particles, mechanical straining becomes a dominant mechanism of colloid retention in soil and aquifer matrices (Bradford et al., 2004). In this study, we focus on microparticles, which are not sufficiently large to experience mechanical straining, but large enough to have non-Brownian trajectories. Particles of this intermediate size range are characterized by transport behavior that are considerably distinct from those of solutes and macroparticles (Molnar et al., 2015).

We explore the pore-scale movement of colloids within various geometries and orientations of soil pore spaces, and various degrees of gravitationally driven and hydrodynamically driven transport, using a particle-tracking model. The large variety of forces acting on colloidal particles, including gravitational, hydrodynamic, electrostatic and Brownian forces, result in highly complex descriptions of particle trajectories at the pore scale. Although colloid attachment and detachment is a primarily electrostatic phenomenon (Adamczyk & Weroński, 1999), the overall matter of whether particles attach to or flow through pore matrices (Seetha et al., 2014), and whether attached particles detach (Burdick et al., 2001), are determined by the particle trajectories resulting from the

overall force balance. Specifically, attachment is much more likely to occur when the forces acting on particles are able to transport them from the bulk fluid to positions close to the pore walls (Johnson, Li, & Assemi, 2007). Once close to the pore walls, the electrostatic forces dominate, and captures the particle if they are sufficiently attractive, leading to attachment.

The movement paths of colloidal particles within porous matrices are also heavily influenced by the geometry of pore throats, as the particles are transported with water flow and experience hydrodynamic forces (Chang et al., 2003). Moreover, the likelihood that gravitation-dominant particle trajectories intersect pore walls (Auset & Keller, 2006) also depends on the pore throat geometry and orientation. Colloid detachment from electrostatic potential minima is contingent on the total force balance acting upon the particle (Bergendahl & Grasso, 2000), which includes hydrodynamic drag (Johnson, Li, & Assemi, 2007) and gravity (Bedrikovetsky et al., 2011), making detachment dependent on pore geometry and orientation as well. Various geometrical models of pore spaces or pore throats exist, such as cylindrical tubes (Seetha et al., 2014), spherical collectors (Gupta & Peters, 1985; Vaidyanathan & Tien, 1988), sphere-in-cells (Mackie et al., 1987), hemispheres-in-cells (Ma et al., 2009), and constricted tubes (Payatakes et al., 1973a). Among these, only the constricted tube and hemisphere-in-cells model simultaneously accounts for the shape, size, and relative positions of the granular material constituting the porous media. Unique to the constricted tube model is that analytical solutions of the flow field are available for various types of constricted tube geometries (Chang et al., 2003), greatly reducing computational requirements and allowing the effects of minor to major variations in constricted tube geometry to be studied. A limitation of the constricted tube model is that it does not explicitly represent flow stagnation zones, where colloid attachment and accumulation in porous media may also occur (Johnson, 2020). Nevertheless, as the constricted tube model has proven suitable for characterizing pore and fracture spaces within rock grain matrices composed of randomly packed spherical grains (Chan & Ng, 1988), we have chosen it for this study. Each individual pore throat, which is connected to an infinite number of other identical pore throats, is depicted as a hollow, constricted tube that represents the space between soil or rock grains forming a soil matrix (Payatakes et al., 1973a).

In this study, we conduct a numerical analysis of colloid deposition influenced by varying degrees of hydrodynamic forces, including hydrodynamic lift, Brownian motion, and significant gravitational forces within constricted tube pore-spaces of various orientations relative to gravity, aiming to clarify the impact of this comprehensive force balance on colloid attachment. We investigate the collection efficiency $\eta$, the probability of a colloid entering a pore space becoming attached as opposed to exiting the space. This efficiency, also referred to as clean-bed collection efficiency in the literature (e.g., Messina et al., 2015; Yao et al., 1971), is widely employed to upscale colloid transport and retention in bulk porous media using continuum models (Elimelech, 1994; Leij et al., 2016) and is relevant to colloid transport through soils (e.g., Nizzetto et al., 2016). Additionally, we analyze the deposition morphology, which represents the locations within the pore where particles adhere. The deposition morphology is crucial in determining the possibility of subsequent remobilization and removal of attached particles, which depends on the hydrodynamic forces acting upon the attached particles. In a constricted tube-shaped pore space, hydrodynamic forces exhibit more significant spatial variations than in simpler pore shapes, such as cylindrical tubes. Therefore, the deposition morphology is also a key factor in evaluating remediation potential and spatial heterogeneity in attached colloid content within soils.

Prior research on attachment in constricted tube models has focused on Brownian particles and smaller non-Brownian particles, whose trajectories are predominantly governed by the interplay between Brownian motion, DLVO interactions, and hydrodynamic drag (Chang et al., 2003, 2008; Chaumeil & Crapper, 2014; Y. Yang et al., 2018), without considering gravitational sedimentation and hydrodynamic lift. Physical models considering these processes, in pore geometries other than the constricted tube model, have been studied in some prior research (e.g., Johnson, 2020; Rasmuson, Erickson, et al., 2019; Yu et al., 2022). For porous media described with the constricted tube model, in addition to Brownian motion, DLVO interactions, and hydrodynamic drag, this research is the first to incorporate several additional processes into a comprehensive characterization of pore-scale particle transport. These processes include (a) a range of constricted tube geometries, (b) the gravitational force and diverse tube orientations in relation to gravity, and (c) the lift force.
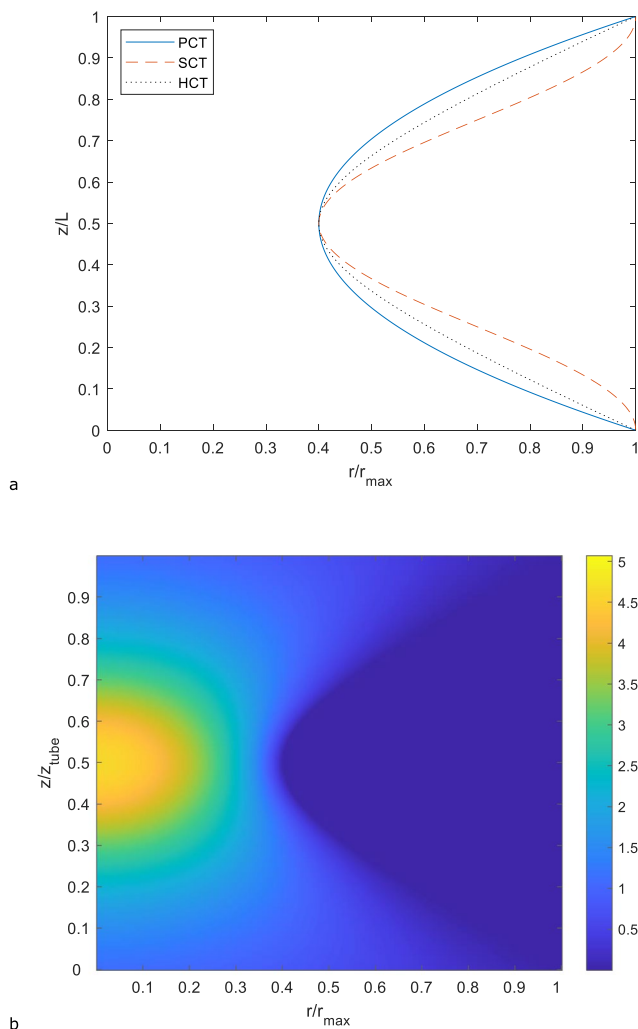
a



b

**Figure 1.** (a) Cross-sectional views of the three-dimensional pore wall geometries of the three constricted pore models, for a pore constriction ratio of 0.4. (b) Magnitudes of fluid velocities in hyperbolic constricted tubes, normalized to the mean axial velocity across the constriction $u_m$.

## 2. Methods

### 2.1. Constricted Tube Model

We investigate the impact of small variations in pore throat shape on particle deposition by analyzing different constricted pore shapes. Given the inherent heterogeneity of pore throats within a soil matrix, it is crucial to ensure that the model's results are applicable to a variety of similar yet distinct pore throat geometries. Therefore, we simulate several three-dimensional axisymmetric constricted tube geometries as defined by Chang et al. (2003), including parabolic (PCT), sinusoidal (SCT), and hyperbolic (HCT) constricted pores. These three constricted pore shapes (Figure 1a) each possess unique characteristics that may influence deposition patterns and the collection efficiency ($\eta$) (Chang et al., 2003). The equations that define the planar cross-sections of these three tube geometries as a function of the maximum tube radius $r_{max}$, constriction radius $r_c$, and constricted tube length $L$, together with the analytical solutions for stream functions and fluid velocities in these three-dimensional constricted tube models under fully saturated conditions as a function of the average axial velocity across the constriction $u_m$, are presented by Chang et al. (2003) in their Equations 1–15, and will not be reproduced here. Laminar flow and no-slip boundary conditions is assumed, which is typical for fluid-material and fluid-particle interactions in groundwater flow (Bear & Cheng, 2010). The boundary conditions used in deriving the analytical solutions for the stream functions and fluid velocities assume that the porous media is composed of an infinite chain of connected constricted tubes, instead of a single freestanding tube, to better represent flow in porous media (Payatakes et al., 1973b). Figure 1a illustrates the three pore wall geometries. Figure 1b illustrates the fluid velocities in HCT, normalized against $u_m$. In the numerical simulations of particle trajectories, the pore wall geometries are rotated around the longitudinal axis to generate a three-dimensional axisymmetric constricted tube, which represent a pore space.

### 2.2. DLVO Interactions

We explicitly account for the electrostatic and short-range interactions between particles and pore walls, collectively referred to as DLVO interactions. Simulating attachment through energy barriers is technically challenging (Pazmino, Trauscht, & Johnson, 2014), and due to the vast parameter space associated with energy barriers and secondary energy minima, we exclude DLVO potentials with energy barriers from our study. Moreover, research suggests that some colloid attachment in porous media under energy barrier conditions may sometimes not actually be caused by attachment, but rather by colloids becoming wedged between matrix grains or trapped in stagnant flow zones (Johnson, Li, & Yal, 2007). In such a case, nanoscale charge heterogeneity may also facilitate attachment under mean-field repulsive conditions, but is beyond the scope of this study, though we note that numerical models that consider this are available for other pore geometries (e.g., Johnson, 2020; Rasmuson, VanNess, et al., 2019). Possible attachment through energy barriers may be characterized by combining the collection efficiency with a sticking efficiency parameter (Lin et al., 2021, 2022), which is at least in the first order independent of the collection efficiency. Thus, we only simulate purely attractive DLVO potentials, representing favorable attachment conditions, to obtain the collection efficiency (Molnar et al., 2015). Accordingly, following Chang et al. (2003), Ma et al. (2013), and Chaumeil and Crapper (2014), we model the DLVO force for an entirely attractive electrostatic interaction using the Van der Waals force ($F_{VDW}$).

### 2.3. Lagrangian Particle Tracking

In this study, we assume a non-crowded environment where the presence of colloid particles does not influence water flow, and we disregard explicit colloid-colloid interactions, given that many important microparticle contaminants such as bacteria and microplastics are typically present in soils in very low volumetric concentrations compared to the pore space (Rafique et al., 2020; Williamson et al., 2017). A solid, spherical particle submerged in a viscous, incompressible fluid passing through a permeable material interacts with both the fluid and the material, experiencing a total force and torque that influences its trajectory. Following Spielman and Fitzpatrick (1973), particles are assumed to be small relative to the pore walls such that particle-wall interactions, including wall effects on hydrodynamic forces, can be characterized as interactions between a sphere and a planar surface.

Lagrangian particle tracking (Mahdavimanesh et al., 2013) is employed to ascertain a particle's path. As particles approach the pore walls, the forces they experience are significantly influenced by the separation distance between the particle and the pore surface, due to the presence of electrostatic interaction forces and the impact of wall effects on hydrodynamic forces. Consequently, even though a cylindrical coordinate system is utilized to calculate flow streamlines and velocities, a local Cartesian coordinate system $(x, y, z)$ is employed for determining forces and interactions between particles and walls, with the wall situated on the $(x, y)$ plane and the particle positioned at $(0, 0, z_p)$. $z_p$ represents the distance from the wall surface to the particle's center. The fluid velocities calculated in cylindrical coordinates are first transformed to the local coordinate system before the hydrodynamic forces acting upon the particles and the resulting particle trajectories are calculated. The trajectories are subsequently converted back to the cylindrical coordinate system, and the particles' new positions are updated, thus completing a single numerical timestep. A particle is considered to be attached when the separation distance becomes zero. Additional information on the transformation between the local and cylindrical coordinate systems, as well as the influence of tube orientation on the gravitational force vector, are presented in Appendix A.

With the above assumptions and methods, the net force acting on a particle is

$$\boldsymbol{F} = \begin{bmatrix} F_x \\ F_y \\ F_z \end{bmatrix} = \boldsymbol{F}_{\text{grav}} + \boldsymbol{F}_{\text{VDW}} + \boldsymbol{F}_{\text{drag}} + \boldsymbol{F}_{\text{lift}} + \boldsymbol{F}_{\boldsymbol{B}} \tag{1}$$

where $\boldsymbol{F}_{\textbf{grav}}$ is the gravitational force, $F_{\text{VDW}}$ is the van der Waal's force (Chang et al., 2003), $\boldsymbol{F}_{\textbf{drag}}$ is the hydrodynamic drag (Adamczyk, 2017), $F_{\text{lift}}$ is the lift force (Saffman, 1965), and $\boldsymbol{F}_{\boldsymbol{B}}$ is the force due to Brownian motion (Adamczyk, 2017). Bolded symbols refer to vector quantities. Following Ma et al. (2009), the DLVO and lift forces only act in the normal direction to the surface. The individual forces in the local coordinate system $(x, y, z)$ are

$$\boldsymbol{F}_{\text{grav}} = \frac{4}{3}\pi a^3 (\rho_p - \rho_f)\boldsymbol{g} \tag{2}$$

$$F_{\text{VDW}} = -\frac{2A}{3a}\left[\frac{1}{\left(H^2 + 2H\right)^2}\right] \tag{3}$$

$$\boldsymbol{F}_{\text{drag}} = 6\pi\mu a F_8 \boldsymbol{u} \tag{4}$$

$$F_{\text{lift}} = 81.2a^2 u_x \sqrt{\mu\rho_f G} \tag{5}$$

$$\boldsymbol{F}_{\boldsymbol{B}} = \sqrt{\frac{2k_B T}{\boldsymbol{M}_{tt}\Delta t}}\boldsymbol{\phi}_{\boldsymbol{B}} \tag{6}$$

Here, $a$ is the particle radius, $\rho_p$ is the particle density, $\rho_f$ is the density of water, $\boldsymbol{g}$ is the gravitational vector (see Appendix A), $A$ is the Hamaker constant, $\mu$ is the viscosity of water, $\boldsymbol{u}$ is the velocity difference between the particle and water, $u_x$ is the $x$-component of $\boldsymbol{u}$, $G$ is the fluid shear rate normal to the wall, $k_B$ is the Boltzmann constant, $T$ is the temperature, $\boldsymbol{\phi}_{\boldsymbol{B}}$ is a random vector with each index uniformly distributed between $-0.5$ and $0.5$, and $\Delta t$ is the numerical timestep. $F_8$ and the other functions $F_i(H)$ ($1 \le i \le 9$) used in this study are hydrodynamic

**Table 1**
*Universal Hydrodynamic Correction Functions (Adamczyk, 2017)*

| | | | |
|---|---|---|---|
| $F_1$ | | $\frac{H(19H+4)}{19H^2+26H+4}$ | |
| $F_3$ | $\frac{0.7431}{0.6376-0.2\ln(H)}$ for $(H < 0.05)$ | $\frac{1}{0.754-0.256\ln(H)}$ for $(0.05 \le H < 0.15)$ | $1 - \frac{0.304}{(1+H)^3}$ for $(H \ge 0.15)$ |
| $F_4$ | $\frac{1}{-(8/15)\ln(H)+0.9588}$ for $(H < 0.1)$ | | $\left(\frac{H}{2.639+H}\right)^{1/4}$ for $(H \ge 0.1)$ |
| $F_6$ | $\frac{0.8436}{0.6376-0.2\ln(H)}$ for $(H < 0.05)$ | $\frac{1}{-(2/5)\ln(H)+0.3817}$ for $(0.05 \le H < 1)$ | $\frac{1}{1+\frac{5}{16(H+1)^3}}$ for $(H \ge 1)$ |
| $F_7$ | $\frac{1}{-(2/15)\ln(H)+0.2526}$ for $(H < 1)$ | | $4(H+1)^2$ for $(H \ge 1)$ |
| $F_8$ | $1.705$ for $(H < 0.1)$ | | $1 + \frac{9}{16}\frac{1}{(H+1)}$ for $(H > 0.1)$ |
| $F_9$ | $0.944$ for $(H < 0.1)$ | | $1 - \frac{3}{16}\frac{1}{(H+1)^3}$ for $(H > 0.1)$ |

correction functions (Table 1), which correct for wall effects on the forces acting upon a particle when it is located close to a pore wall.

The relative separation distance between the particle and the wall is

$$H = \frac{h}{a} = \frac{z_p - a}{a} \tag{7}$$

where $h$ is the absolute separation distance. The translational mobility tensor $\boldsymbol{M}_{tt}$ is given by

$$\boldsymbol{M}_{tt} = \begin{bmatrix} M_{\parallel} & 0 & 0 \\ 0 & M_{\parallel} & 0 \\ 0 & 0 & M_{\perp} \end{bmatrix} \tag{8}$$

$$M_{\parallel} = \frac{F_{4p}}{6\pi\mu a} \tag{9}$$

$$M_{\perp} = \frac{F_1}{6\pi\mu a} \tag{10}$$

$$F_{4p} = \frac{F_4}{1 - \frac{2}{3}\frac{F_4 F_6}{F_7^2}} \tag{11}$$

The Langevin equation describes the relationship between the forces acting on the particle and the resulting translational velocity (Felderhof & Sellier, 2012). In discrete form, the Langevin equation that describes the particle's trajectory in the local coordinate system $(x, y, z)$ is

$$\Delta\overline{\boldsymbol{x}} = \boldsymbol{M}_{tt}\boldsymbol{F}\Delta t + \begin{bmatrix} z_p F_3 G \\ 0 \\ 0 \end{bmatrix}\Delta t + k_B T(\nabla\boldsymbol{M}_{tt})\Delta t \tag{12}$$

where the total force $\boldsymbol{F}$ acting on the particle (including the Brownian force) is given by Equation 1, the second term on the right accounts for the effects of shear torque for simple shear flow parallel to a planar surface, and the third term accounts for wall effects on Brownian motion (Adamczyk, 2017; De Corato et al., 2015; Warszyński, 2000).

## 2.4. Simulation Scenarios

Figure 2 illustrates the average magnitude of forces impacting particles within the bulk fluid, with respect to the particle radius. As the particle radius grows, the gravitational force's magnitude increases more rapidly than the
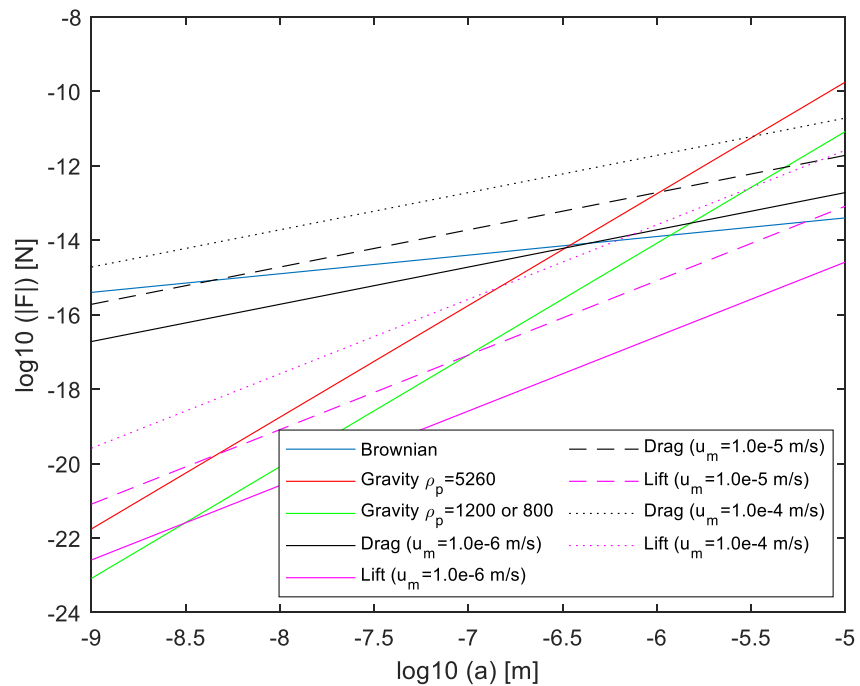
**Figure 2.** Absolute magnitudes of forces as a function of particle size. The drag and lift forces are calculated based on a velocity difference between the water and particles equal to the average axial velocity $u_m$, and based on the average shear rate at the constriction.

hydrodynamic drag force, which in turn, increases faster than the Brownian force. This is due to the following proportionality relationships, with $\boldsymbol{F}_{\mathbf{grav}} \propto a^3$, $\boldsymbol{F}_{\mathbf{drag}} \propto a$, and $\boldsymbol{F}_B \propto \sqrt{a}$. Consequently, the force equilibrium influencing particles in the bulk fluid relies heavily on the particle radius.

Parameter values common to all selected scenarios are the maximum tube radius $r_{\max} = 50$ μm, constriction radius $r_c = 20$ μm, constricted tube length $L = 125$ μm, water density $\rho_f = 1{,}000$ kg/m³, water viscosity $\mu = 0.001$ Pa/s, and temperature $T = 298$K. This pore size range was chosen as it is representative of sands, and silts, and some coarser clays, while also experiencing laminar flow under environmental fluxes (L. Chen et al., 2019). An explicit numerical scheme is used, with time steps ranging between $5 \cdot 10^{-5}s \leq \Delta t \leq 5 \cdot 10^{-3}s$ depending on the scenario. The timesteps were chosen to be much larger than the particle's momentum relaxation time equal to $\frac{2\rho_p a^2}{9\mu}$, in order for the Brownian force to be accurately simulated, yet small enough so that the hydrodynamic forces are approximately constant throughout each timestep (Nelson & Ginn, 2005).

Based on Figure 2, we selected 12 combinations of non-Brownian microparticle size and average fluid velocity as the scenarios to be modeled, which are listed in Table 2. In each simulated scenario, 50,000 non-interacting particles are uniformly distributed over the pore opening area and introduced into the capillary at an initial velocity matching the flow field. The range of fluid velocities investigated in the 12 scenarios correspond roughly to pedon-scale fluxes of 1 to 100 mm/hr: a range representative of environmental flows in soil matrices and fractures, saturated and unsaturated. We did not simulate scenarios with fluid velocities smaller than this range because then, $\boldsymbol{F} \sim \boldsymbol{F}_{\mathbf{grav}}$ for large particles, and $\boldsymbol{F} \sim \boldsymbol{F}_B$ for small particles (Figure 2), reducing the problem to a pure sedimentation or diffusion problem respectively. $\boldsymbol{F}_{\mathbf{lift}}$ is typically much smaller than $\boldsymbol{F}_{\mathbf{grav}}$, $\boldsymbol{F}_{\mathbf{drag}}$, $\boldsymbol{F}_B$ (Figure 2) except under larger fluid velocities; additional scenarios created specifically to study the effects of lift are discussed in detail in Section 3.6.

Scenarios A to G represent dense mineral colloids such as iron oxide, scenarios H to J represent light-but-denser-than-water particles such as heavier microplastics, and scenarios K to L represent buoyant particles such as light microplastics (Kooi & Koelmans, 2019). The values of the Hamaker constant chosen here are representative of colloid contaminants found in the environment: polystyrene microplastics, bacteria, and mineral particles in water and sand have around $A = 1 \cdot 10^{-20}$ J, $A = 5 \cdot 10^{-21}$ J, and $A = 5 \cdot 10^{-20}$ J, respectively (Bradford et al., 2018;

**Table 2**
*Parameters and Collection Efficiencies of Simulated Scenarios*

| Scenario | A | B | C | D | E | F | G | H | I | J | K | L |
|---|---|---|---|---|---|---|---|---|---|---|---|---|
| $u_m$ (m/s) | $1 \cdot 10^{-4}$ | $1 \cdot 10^{-5}$ | $1 \cdot 10^{-5}$ | $1 \cdot 10^{-6}$ | $1 \cdot 10^{-6}$ | $1 \cdot 10^{-6}$ | $1 \cdot 10^{-6}$ | $1 \cdot 10^{-6}$ | $1 \cdot 10^{-6}$ | $1 \cdot 10^{-6}$ | $1 \cdot 10^{-6}$ | $1 \cdot 10^{-6}$ |
| $a$ (m) | $1 \cdot 10^{-6}$ | $1 \cdot 10^{-5.5}$ | $1 \cdot 10^{-6}$ | $1 \cdot 10^{-5.5}$ | $1 \cdot 10^{-6}$ | $1 \cdot 10^{-6.5}$ | $1 \cdot 10^{-7}$ | $1 \cdot 10^{-5.5}$ | $1 \cdot 10^{-6}$ | $1 \cdot 10^{-6.5}$ | $1 \cdot 10^{-6}$ | $1 \cdot 10^{-6.5}$ |
| $\rho_p$ (kg/m³) | $5.26 \cdot 10^3$ | $5.26 \cdot 10^3$ | $5.26 \cdot 10^3$ | $5.26 \cdot 10^3$ | $5.26 \cdot 10^3$ | $5.26 \cdot 10^3$ | $5.26 \cdot 10^3$ | $1.2 \cdot 10^3$ | $1.2 \cdot 10^3$ | $1.2 \cdot 10^3$ | $0.8 \cdot 10^3$ | $0.8 \cdot 10^3$ |
| $A$ (J) | $5 \cdot 10^{-20}$ | $5 \cdot 10^{-20}$ | $5 \cdot 10^{-20}$ | $5 \cdot 10^{-20}$ | $5 \cdot 10^{-20}$ | $5 \cdot 10^{-20}$ | $5 \cdot 10^{-20}$ | $1 \cdot 10^{-20}$ | $1 \cdot 10^{-20}$ | $1 \cdot 10^{-20}$ | $1 \cdot 10^{-20}$ | $1 \cdot 10^{-20}$ |
| Force balance | $F_d > F_g > F_b$ | $F_g > F_d > F_b$ | $F_g \approx F_d > F_b$ | $F_g > F_d > F_b$ | $F_g > F_d > F_b$ | $F_g \approx F_d \approx F_b$ | $F_b > F_d > F_g$ | $F_g > F_d > F_b$ | $F_g \approx F_d > F_b$ | $F_d \approx F_b > F_g$ | $F_g \approx F_d > F_b$ | $F_d \approx F_b > F_g$ |
| Settling number $S$ | $9.3 \cdot 10^{-2}$ | $9.3$ | $9.3 \cdot 10^{-1}$ | $93$ | $9.3$ | $9.3 \cdot 10^{-1}$ | $9.3 \cdot 10^{-2}$ | $4.4$ | $4.4 \cdot 10^{-1}$ | $4.4 \cdot 10^{-2}$ | $-4.4 \cdot 10^{-1}$ | $-4.4 \cdot 10^{-2}$ |
| Collection efficiencies | | | | | | | | | | | | |
| PCT, $\phi = 0$ | 0.48 | 0.7 | 0.63 | 0.75 | 0.75 | 0.64 | 0.50 | 0.70 | 0.60 | 0.46 | 0.49 | 0.38 |
| SCT, $\phi = 0$ | 0.40 | 0.67 | 0.58 | 0.74 | 0.73 | 0.59 | 0.39 | 0.67 | 0.53 | 0.35 | 0.40 | 0.28 |
| HCT, $\phi = 0$ | 0.42 | 0.68 | 0.6 | 0.75 | 0.74 | 0.61 | 0.43 | 0.69 | 0.56 | 0.39 | 0.43 | 0.31 |
| PCT, $\phi = 45$ | 0.45 | 0.99 | 0.64 | 1 | 1 | 0.65 | 0.48 | 0.96 | 0.58 | 0.45 | 0.66 | 0.40 |
| SCT, $\phi = 45$ | 0.35 | 0.98 | 0.57 | 1 | 1 | 0.58 | 0.38 | 0.90 | 0.50 | 0.34 | 0.56 | 0.30 |
| HCT, $\phi = 45$ | 0.38 | 0.99 | 0.60 | 1 | 1 | 0.61 | 0.42 | 0.94 | 0.54 | 0.38 | 0.63 | 0.33 |
| PCT, $\phi = 90$ | 0.44 | 1 | 1 | 1 | 1 | 1 | 0.48 | 1 | 0.66 | 0.43 | 0.66 | 0.43 |
| SCT, $\phi = 90$ | 0.36 | 1 | 0.91 | 1 | 1 | 0.92 | 0.37 | 1 | 0.57 | 0.33 | 0.57 | 0.33 |
| HCT, $\phi = 90$ | 0.38 | 1 | 0.99 | 1 | 1 | 0.99 | 0.41 | 1 | 0.62 | 0.36 | 0.62 | 0.36 |
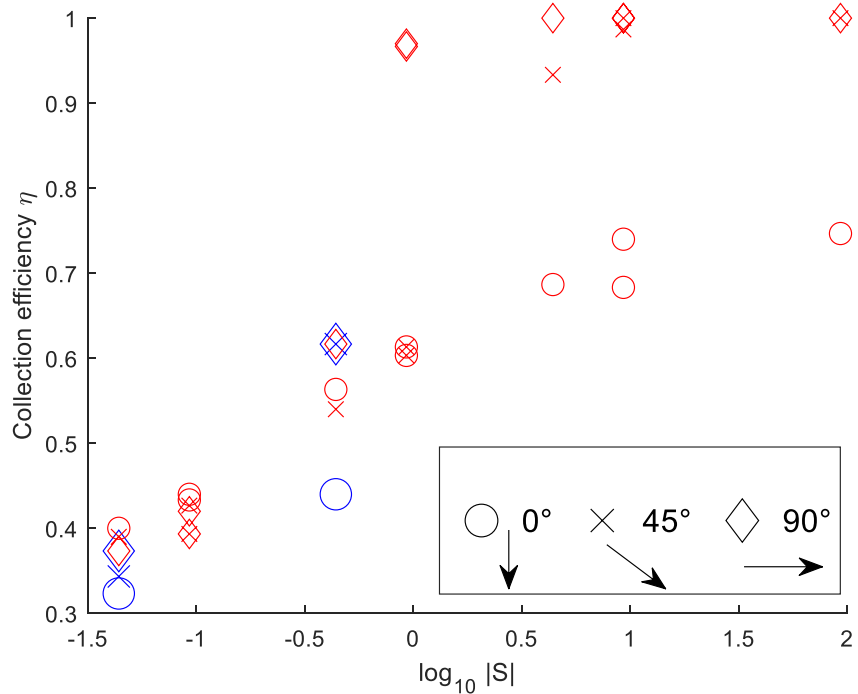
**Figure 3.** Scatter plot of collection efficiencies against $\log_{10}|S|$ for three tilt angles relative to the vertical, averaged over the three constricted tube shapes. Red markers represent the scenarios with heavier-than-water particles, and blue markers (larger-sized for visibility) represent scenarios with buoyant particles. Arrows in the legend illustrate the axial direction of the constricted tube and the mean direction of flow.

Faure et al., 2011; Shen et al., 2018). These scenarios are simulated for all three constricted tube geometries, and for three different tube orientations (Table 2). The three tube orientations are given in terms of angle of deviation $\phi$ from the base case where the axial length of the tube and the middle streamlines run vertically downwards, and are $\phi = 0°$ (vertical downflow), 45° (diagonal downflow), and 90° (horizontal).

## 3. Results and Discussion

### 3.1. Collection Efficiencies

Both $\eta$ and the deposition morphology appear to be primarily influenced by the comparative intensities of gravitational (Equation 2) and hydrodynamic (Equation 4) forces. As a result, we introduce a dimensionless parameter, the settling number ($S$), to measure the relative strengths of these forces.

$$S = \frac{\boldsymbol{F}_{\text{grav}}}{\langle \boldsymbol{F}_{\text{drag}} \rangle} = \frac{2a^2 g(\rho_p - \rho_f)}{9\mu u_m} = \frac{a^2}{u_m} S_c \tag{13}$$

where $S_c$ is defined as $\frac{2g(\rho_p - \rho_f)}{9\mu}$, and the sharp brackets indicate an average $\boldsymbol{F}_{\text{drag}}$ computed assuming that a fluid flowing at a velocity of $u_m$ acts on the particle. Wall effects on particle trajectories are insignificant in the bulk fluid and thus ignored in the settling number, meaning that all $F_i$ are set equal to 1. Essentially, $S$ is the ratio of gravitational force over the average hydrodynamic drag force. Values of $S$ for the various simulated scenarios are listed in Table 2, spanning five orders of magnitude.

Figure 3 reveals that $\eta$ for denser-than-water scenarios (red markers) with similar $\log_{10}|S|$ and tube geometry are highly similar. Note that the scenarios represented by blue markers have buoyant particles, which means that they have negative-valued $S$. Several trends can be observed amongst the denser-than-water scenarios in Figure 3: (a) As $|S|$ increases, $\eta$ increases. (b) As the constricted tube orientation is increasingly tilted from the vertical, the effect of point 1 becomes stronger. (c) In vertical capillaries, once $|S|$ increases beyond some threshold value (around $|S| \sim 1$ in this study), $\eta$ is no longer affected by further increases in $|S|$. This occurs as particles entering

the pore close to its center are predominantly influenced by gravitational and drag forces, which guide the particle directly toward the pore exit, thereby preventing attachment. (d) Table 2 shows that for $|S| \geq 10$, $\eta$ is much more significantly affected by the tube orientation than its geometry. Conversely, for $|S| \leq 0.1$, $\eta$ are affected by the tube's geometry and orientation to a similarly small extent. The above implies that tube geometry and orientation both have small impacts on attachment for $|S| \ll 1$, but attachment is predominantly determined by the tube orientation for $|S| \gg 1$. This essentially clarifies that the shape of the pore-space influences advection-based deposition by altering flow patterns, while the tube orientation impacts sedimentation driven by gravity. For S that approaches zero, previous studies that omit gravity apply (e.g., Chang et al., 2008; Chaumeil & Crapper, 2014; Y. Yang et al., 2018). For $S$ approaching infinity, pure gravitational sedimentation applies, and advection becomes irrelevant.

Figure 3 also demonstrates that $S$, along with tube orientation, account for most of the variability in $\eta$. Other factors contributing to trajectory generation, such as the hydrodynamic torque, DLVO interactions, and Brownian motion, explain only a minor portion of the variance in $\eta$. In addition, Table 2 also shows that the effects of tube geometry on $\eta$ are appreciable but small, being less than 0.1 across all scenarios. Although Brownian and DLVO forces differ across similar situations, their impact on $\eta$ is minimal, especially the DLVO force. For instance, larger particles experience a stronger DLVO force as their larger surface area allows for increased interaction between the electric charges of the particles and pore walls. Despite the considerable difference in Brownian and DLVO forces between scenarios A and G due to particle size, $\eta$ remains similar in both cases. The same can be said for other subsets of scenarios with similar $S$. The DLVO attraction force $F_{\mathrm{VDW}}$ (Equation 3) diminishes rapidly with increasing particle-wall separation distance, and thus significantly contributes to the overall force balance of particles only when they are in close proximity to the wall. This is confirmed in the numerical simulations, where the strength of the DLVO attraction appears to have a relatively minor impact on the trend displayed in Figure 3 despite varying between $A = 1 \cdot 10^{-20}$ J to $A = 5 \cdot 10^{-20}$ J across the scenarios. Furthermore, additional simulations of scenario A with a hundredfold increase to $A = 5 \cdot 10^{-18}$ J resulted in $\eta$ increasing by no more than 0.01. Consequently, particle collection efficiencies and deposition patterns can be summarized to primarily rely on the balance between hydrodynamic and gravitational forces acting upon the colloids. Note however that if unfavorable attachment conditions (e.g., repulsive DLVO interactions) were instead considered, the attached fraction would be significantly affected by the hydrodynamic torque, and both the mean-field and small-scale local heterogeneities of the DLVO interaction potential (Pazmino, Trauscht, Dame, & Johnson, 2014; Pazmino, Trauscht, & Johnson, 2014; Rasmuson, VanNess, et al., 2019).

The simulations of the 12 scenarios were repeated twice, and the collection efficiency across realizations of each scenario had a mean difference of $\pm 0.0001$, even though the trajectories were not completely deterministic due to Brownian motion, implying that the number of particles per simulation (50,000) is sufficient. Further additional simulations with Brownian motion omitted show that if Brownian motion is omitted from a simulation, the collection efficiency is different by at most $\pm 0.02$ (scenario F, I) and $\pm 0.05$ (scenario G, J, L) compared to the same scenarios with Brownian motion included. No generalizations could be made about the sign of the difference (negative or positive), which depended on the specific scenario, though in most cases omitting Brownian motion caused the collection efficiency to be overestimated. Brownian motion had no appreciable effect in the other scenarios.

Hence, even in scenarios G, J, L, the scenarios where Brownian motion has the most significant contributions to the force balance (Table 2), Brownian motion lacks the combined strength and directionality to significantly affect deposition outcomes. It is well-known that unbiased random-walk diffusion leads to a mean displacement proportional to $\sqrt{t}$, thus the traversal time of the particles longitudinally through the constricted tube may have been too fast relative to the radial diffusion of particles, for diffusion to have a significant effect on collection efficiencies. Anisotropic Brownian motion occurs only near tube walls, where wall effects cause a biased random walk away from the wall. However, at such close proximities to the walls, DLVO forces dominate, possibly rendering the anisotropic effect negligible.

An outlier to the small effect of Brownian motion applies to scenario K (only in vertical tubes), where omitting Brownian motion leads to an underestimation of the collection efficiency by 0.15 (~30% in relative terms). This is because the buoyancy of the particles counteracts the already-slow downwards fluid velocity, which causes particles to traverse the tube very slowly, allowing particles ample time to diffuse toward the pore walls. This
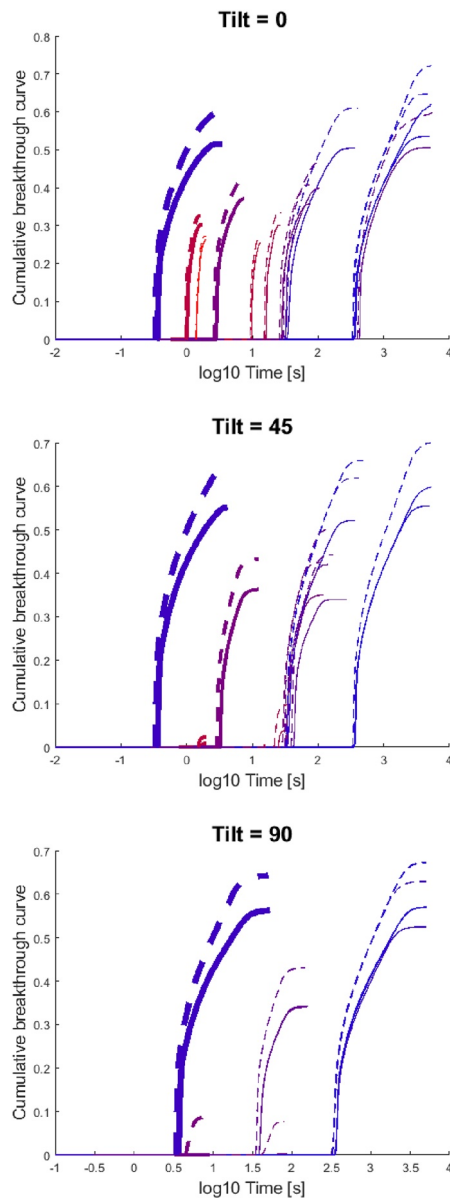
**Figure 4.** Cumulative breakthrough fractions of particles that flow through the pore throat without being attached, as a function of log time, for the 12 scenarios. Solid lines refer to PCT, and dashed lines to SCT. Red lines represent scenarios with larger $|S|$, and blue lines represent scenarios with smaller $|S|$. Thicker lines represent scenarios with larger fluid velocities, and thinner lines the opposite.

result for scenario K is also an exception to the general notion that Brownian motion is unimportant in the transport of particles with sizes larger than the order of 100 nm.

### 3.2. Effects of Constricted Tube Geometry on $\eta$

For scenarios D, E, H, where the gravitational force dominates all other forces on average, the results show that hydrodynamic forces are still sufficiently strong to prevent a large number of attachments that would have occurred in the absence of fluid flow. Given that the constriction ratio $r_c/r_{max}$ of the tube is 0.4, and since the particles are evenly distributed at the inlet of the pore mouth, the collection efficiency would be approximately $1 - 0.4^2 = 0.84$ in vertically oriented tubes if particle trajectories were determined solely by gravitational sedimentation. With only DLVO forces added, the collection efficiency would then be larger than 0.84. As the simulated collection efficiencies for scenarios D, E, H in vertical tubes are clustered around 0.7, it can be inferred that the hydrodynamic forces prevented a significant fraction ($>0.1$) of particles from attaching. The role of pore shape on particle fate is also evident in the remarkable results for horizontally oriented tubes in scenario C and scenario F ($F_g \approx F_d$), where around 0% of particles exit the pore for PCT and HCT but around 8% do for SCT. Hence, small differences in tube geometry may lead to appreciable differences in particle transport.

In agreement with Chang et al. (2003)'s results for Brownian particles, we find that the collection efficiency for non-Brownian particles subject to gravitational sedimentation and a fully attractive DLVO interaction is also largest for PCT, then HCT, then SCT (Table 2), for all simulated scenarios. The breakthrough of non-attached particles at the pore outlet occurs earliest for SCT, and latest for PCT (Figure 4). Given that $u_m$ is consistent across all three tube geometries in this comparison, this suggests that non-attached particles encounter the greatest average axial velocity in SCT, which in turn implies that attached particles experience the lowest average axial velocity in SCT. Note that particle deposition becomes less favorable as fluid velocities increase, since the hydrodynamic drag force vector is perpendicular to the DLVO force vector. The fact that bound particles exhibit the highest average velocity in PCT and the lowest in SCT reinforces that colloid deposition is most favorable in PCT and least favorable in SCT. In other words, PCT is more conducive to deposition than SCT partly because PCT can capture particles moving at higher axial velocities. Another reason is that for identical pore-size parameters, PCT has the smallest pore-space volume (Figure 1a).

### 3.3. Effects of Constricted Tube Geometry on Deposition Morphology

Figure 5 illustrates that the spatial distribution of attached particles significantly depends on the capillary orientation and differs among the three constricted tube geometries. The deposition pattern of HCT demonstrates a behavior that generally falls between PCT and SCT, similar to the collection efficiency. Figure 5 indicate that particles subjected to the force balance simulated in this study tend to attach at the axial ends of the constricted tube, especially the upstream extremity, with the most significant effect in PCT and the least in SCT. This occurs because gravitational sedimentation encourages particles to attach preferentially to pore wall regions with a slope relative to the vertical. SCT exhibits a high density of attached particles at a quarter of the tube depth, where particles are directed toward the pore wall by streamlines. Furthermore, in vertical tubes, buoyant particles may attach close to the pore outlet, which does not occur for heavier-than-water particles. Another important general result evident in Figure 5 is that scenarios with smaller $|S|$ (bluer lines) have larger fractions of attached particles concentrated at the tube extremities (thinner lines). Previous studies have shown that for non-Brownian
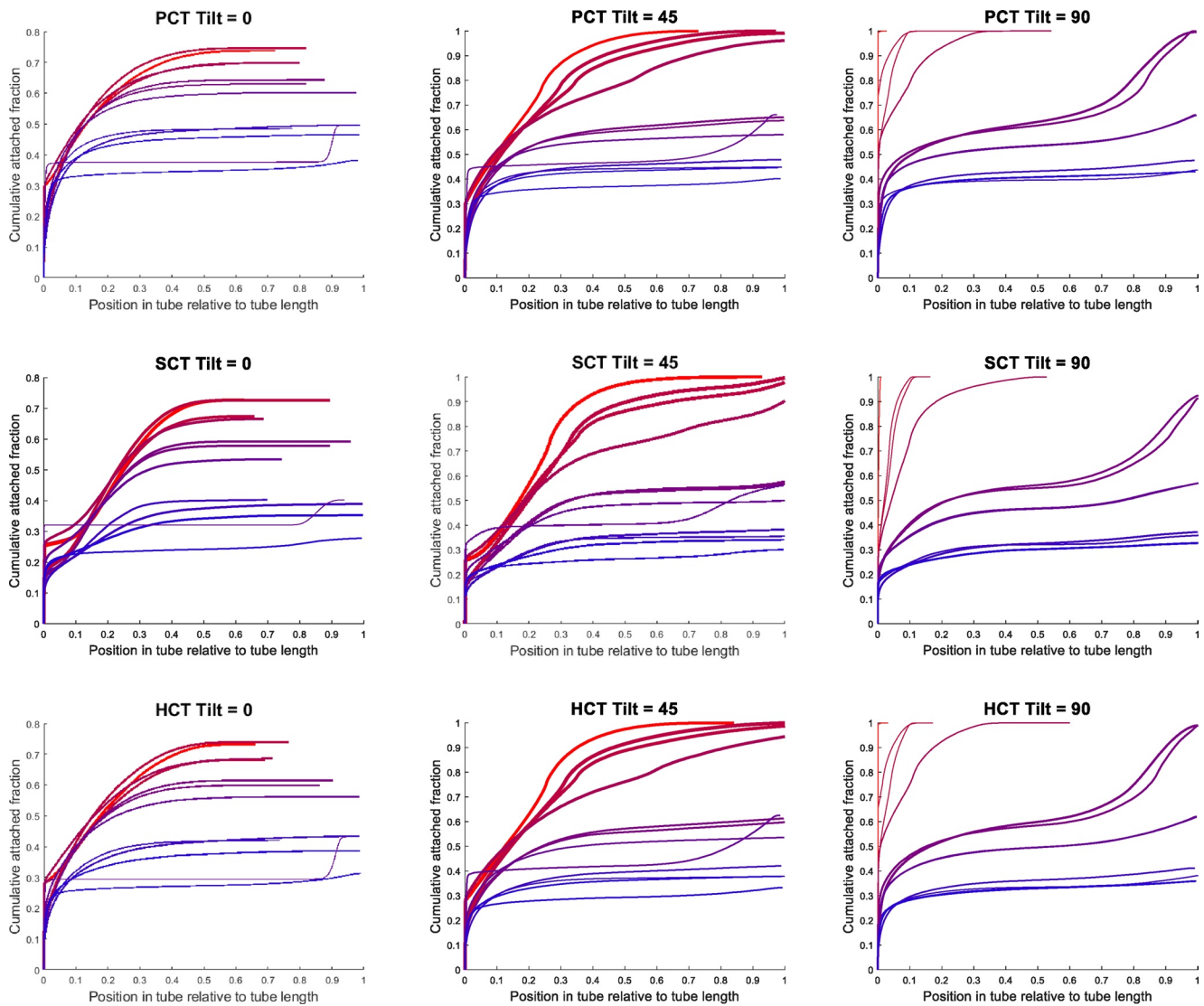
**Figure 5.** Cumulative attached fraction of particles as a function of relative position in constricted tube, for the 12 scenarios. Red lines represent scenarios with larger $|S|$, and blue lines represent scenarios with smaller $|S|$. Thicker lines represent scenarios with a larger fraction of deposited particles located in the middle portion of the constricted tube (relative position between 0.25 and 0.75).

agglomerates of particles not influenced by gravity, attachment tends to also take place away from the constriction of a PCT tube (Chang et al., 2008; Chaumeil & Crapper, 2014). In this study, we show that the same applies when agglomeration is not considered, and also when gravitational sedimentation and buoyancy is significant. This is in contrast to Brownian particles, which by nature of their diffusive transport behavior attach uniformly to the pore walls.

### 3.4. Effects of Constricted Tube Orientation on $\eta$

In scenarios B, C, D, E, F, H where the gravitational force on particles significantly outweighs the hydrodynamic force, adjusting the tube from a vertical to a horizontal position enhances the collection efficiency to its maximum value of 1. The peak efficiency is achieved at a tilt exceeding 45° in scenarios C, F, H while in scenarios B, D, E, it occurs at a tilt under 45°. Scenarios C, F exhibit the weakest gravitational force relative to hydrodynamic forces among these five scenarios. Hence, it can be deduced that as the gravitational force's dominance increases, a larger sinking velocity is more quickly attained by the particles, and therefore a smaller tilt angle is needed to reach the highest collection efficiency. In comparison, the findings reveal that the collection efficiencies in

scenarios A, G are barely affected by the constricted tube's orientation. This is due to gravity being a minor factor in determining a particle's path in these scenarios. Consequently, when hydrodynamic forces dominate over gravitational forces, the pore's orientation does not significantly influence particle trajectories.

The trend between $|S|$ and $\eta$ also applies to buoyant particles (Figure 3), except for a single outlier. The blue circle outlier in Figure 3 relates to scenario K in vertical tubes, previously also identified as an outlier in Section 3.1. In this scenario, $|S|$ alone does not describe particle fate: buoyancy counteracts hydrodynamic drag as the streamlines primarily point vertically downwards, which causes other forces (e.g., lift, Brownian) to play relatively amplified roles in determining particle trajectories. Furthermore, when controlling for the same density difference with water (i.e., identical $|\rho_p - \rho_f|$), whether buoyant particles (scenarios K, L) have a higher or lower $\eta$ than heavier-than-water particles (scenarios H, I, J), is controlled by the tube orientation (Table 2). This is evident when comparing $\eta$ of scenarios K, L with I, J. Buoyancy decreases $\eta$ in vertical tubes, as it moves particles away from the wall. In diagonal tubes, buoyancy can increase or decrease $\eta$, depending on the specific force balance scenario. In horizontal tubes, buoyant and heavier-than-water particles with identical $|\rho_p - \rho_f|$ have the same collection efficiency as the problems are physically identical.

### 3.5. Effects of Constricted Tube Orientation on Deposition Morphology

Figure 5 shows that majority of attached particles were found near the pore extremities, especially the entrance, whereas few particles attached around the middle (relative position between 0.25 and 0.75), especially for smaller $S$. The clustering of attached particles near the extremities is strongest in horizontal tubes, then vertical, and weakest in diagonal tubes. In vertical tubes, minimal particle attachment occurred in the latter half of the constricted tube, as both hydrodynamic and gravitational forces counteracted attachment. Consequently, the collection efficiencies and deposition patterns of scenarios with $S > 1$ in vertically oriented tubes were similar, with most particles adhering to the upper quarter of the pore throat.

In horizontally oriented pores, scenarios B, C, D, and E demonstrated comparable collection efficiencies. In scenarios D and E, characterized by low fluid velocities, the majority of particles attached to the upper quarter of the horizontal pore throat. Conversely, in horizontally oriented tubes with higher fluid velocities, such as scenarios B and C, particles predominantly settled at the constricted tube's two ends. Distinct from the other two orientations, horizontally oriented pores exhibited a higher probability of particle deposition near the tube outlet due to low fluid velocities in that area, enabling gravitational sedimentation to bring particles closer to the pore wall. The underlying reason for these observations is that gravity significantly influences deposition in these simulated scenarios, and most particles adhere to pore regions where gravity overpowers hydrodynamic forces. At the pore extremities, which possess larger cross-sectional areas, fluid velocities are low and hydrodynamic forces are weak, causing particles to preferentially attach to the constricted tube's axial extremities. Hence, in horizontal pores, particles' axial velocities significantly decrease as they approach the outlet, resulting from the reduced fluid velocity, which allows gravity to draw particles toward the pore wall. Additionally, colloid particles spend less time traversing regions with high fluid velocities due to rapid advection. Essentially, the result is that colloid particles tend to deposit in areas with low fluid velocities, as the tangential drag force is small, making gravity and the DLVO force more prominent in the force balance. As previously noted, the relative concentration of attached particles in the pore extremities is most remarkable for smaller $|S|$ (lighter particles), because the smaller gravitational forces they experience are overcome by hydrodynamic forces in a larger region around the pore constriction.

### 3.6. Hydrodynamic Lift

It was previously thought that in the absence of density differences between particles and the fluid, migrating particles adhered to streamlines. However, recent research has shown on the contrary that particles migrate across streamlines due to hydrodynamic lift, a phenomenon referred to as inertial focusing (Di Carlo et al., 2007). This process propels particles away from pore walls under laminar flow, leading to lower collection efficiencies. Extensive research has been conducted to understand the effect of lift on particle trajectories in cylindrical tubes (e.g., B. H. Yang et al., 2005). However, its impact in the constricted tube geometries used in this study remains relatively unexplored, an aspect we aim to briefly investigate here.

To gain insights into the interactions between varying pore constriction ratios ($r_c/r_{max}$), lift forces, and particle density, additional simulations in HCT pores were performed with parameter values as follows: $r_{max} = 300 \ \mu m$,

$L = 1,000 \, \mu m$, $u_m = 2 \cdot 10^{-4}$ m/s, $a = 5 \cdot 10^{-6}$ m, and $A = 5 \cdot 10^{-20}$ J. Particle densities used previously, 5,260, 1,200, 800 kg/m³, were also implemented here, resulting in $S$ values approximately between 0.1 and 1, implying that gravity plays a significant, albeit non-dominant role. These parameter combinations, characterized by relatively large fluid velocities and particle sizes, suggest a more substantial contribution of $F_{lift}$ to the total force compared to other scenarios, thus providing a clearer understanding of the effects of hydrodynamic lift. Simulations were conducted in tube geometries that were considerably wider and longer than those in other scenarios, ensuring the model assumption that the pore space is significantly larger than the particle remained valid, even within the constricted region in simulations with small $r_c/r_{max}$. Constriction ratios were simulated within the range $0.1 \leq r_c/r_{max} \leq 0.9$.

As anticipated, scenarios with smaller constriction ratios demonstrated larger collection efficiencies (Figure 6a). Consistent with previous findings, a decrease in particle density led to a decrease in collection efficiency (Figure 6a). By repeating each simulation without the lift force, we could discern the influence of the lift force on collection efficiencies, which did not significantly differ across the constricted tube geometries. For particles with $\rho_p = 5,260$ kg/m³, the collection efficiencies in simulations conducted without lift were strikingly similar to those that incorporated lift, irrespective of the constriction ratio (Figure 6b). In the case of buoyant particles with $\rho_p = 800$ kg/m³, absolute differences of up to 0.09 (a relative difference of 33% (Figure 6b)) were noted. For particles with $\rho_p = 1,200$ kg/m³ and $\rho_p = 800$ kg/m³, the effect of lift was significantly dependent on the constriction ratio (Figure 6b).

A prominent trend observed in Figure 6b indicates that the most notable differences due to hydrodynamic lift tend to occur with buoyant particles in non-vertical tubes with smaller constriction ratios. Lighter particles experience smaller $F_{grav}$, which means $F_{lift}$ has a larger contribution to $F$. Lift has a larger effect with smaller constriction ratios, where $F_{lift}$ is larger because the shear rate is higher, and streamlines are more densely packed in space so particles have to travel shorter distances to cross streamlines. In non-vertical tubes, where gravitational settling is more significant because $F_{grav}$ points toward larger portions of the tube surface area, lift is more likely to allow lighter particles to overcome gravitational settling. As an exception, this trend is broken in constricted tubes with the smallest constriction ratio of 0.1, because the very small constrictions amplify the effect of Brownian motion in diffusing particles toward the capture zone of the pore walls, which then causes lift to have a relatively small impact (11%) on trajectories. When the simulations with a constriction ratio of 0.1 were repeated with Brownian motion disabled, the aforementioned trend did not break, and omitting the lift force led to a 35% overestimation of the collection efficiency. Hence, here we have shown that Brownian motion and hydrodynamic lift may cause large-sized interaction effects in some situations (light particles, tight constrictions) even though both are minor components of the force balance, even for relatively large particles with 10 micron diameters.

Figures 6c–6f reveal that attached particles are predominantly concentrated at the axial ends of the tubes (thin lines) when the constriction ratio is smaller (blue lines), a phenomenon that would be overlooked by cylindrical pore models. The absence of lift force also results in varied deposition morphologies, particularly for lighter particles (compare Figure 6c with Figure 6d). Figures 6c–6f also illustrate that the effects of lift on deposition and deposition morphology mainly occur in the downstream half of the tube, especially in non-vertical tubes (Figures 6c and 6e), but to a lesser extent in vertical tubes (Figure 6f). The variation in deposition morphology was minimal for vertical tubes (Figure 6f), or for dense particles with $\rho_p = 5,260$ kg/m³.

Therefore, the impact of lift force on the fate of particles is particularly relevant for light and buoyant particles in soils. These soils comprise pore throats of diverse orientations, especially when the porosity is small or heterogeneous (i.e., the presence of tighter constrictions). The interplay between hydrodynamic lift and non-cylindrical tube geometries is crucial for characterizing buoyant particle transport at the pore scale. If overlooked, it could lead to significantly lower collection efficiencies than otherwise predicted. Although the fluid velocities and pore sizes simulated in these additional scenarios may be rather large for typical environmental flows in soil matrices, they are relevant to flow in fractures, macropores, and high-conductivity conduits. If such preferential flow zones are present, the advection of contaminants may be routed primarily through them (Tang & Van Der Zee, 2022).

## 4. Implications for the Detachment and Remobilization of Attached Particles

### 4.1. Critical Velocity for Mechanical Remobilization

Attached particles may detach from an attachment site through three hydrodynamically driven mechanisms, lifting, sliding, and rolling. All three mechanisms depend on hydrodynamic torques overcoming the adhesive
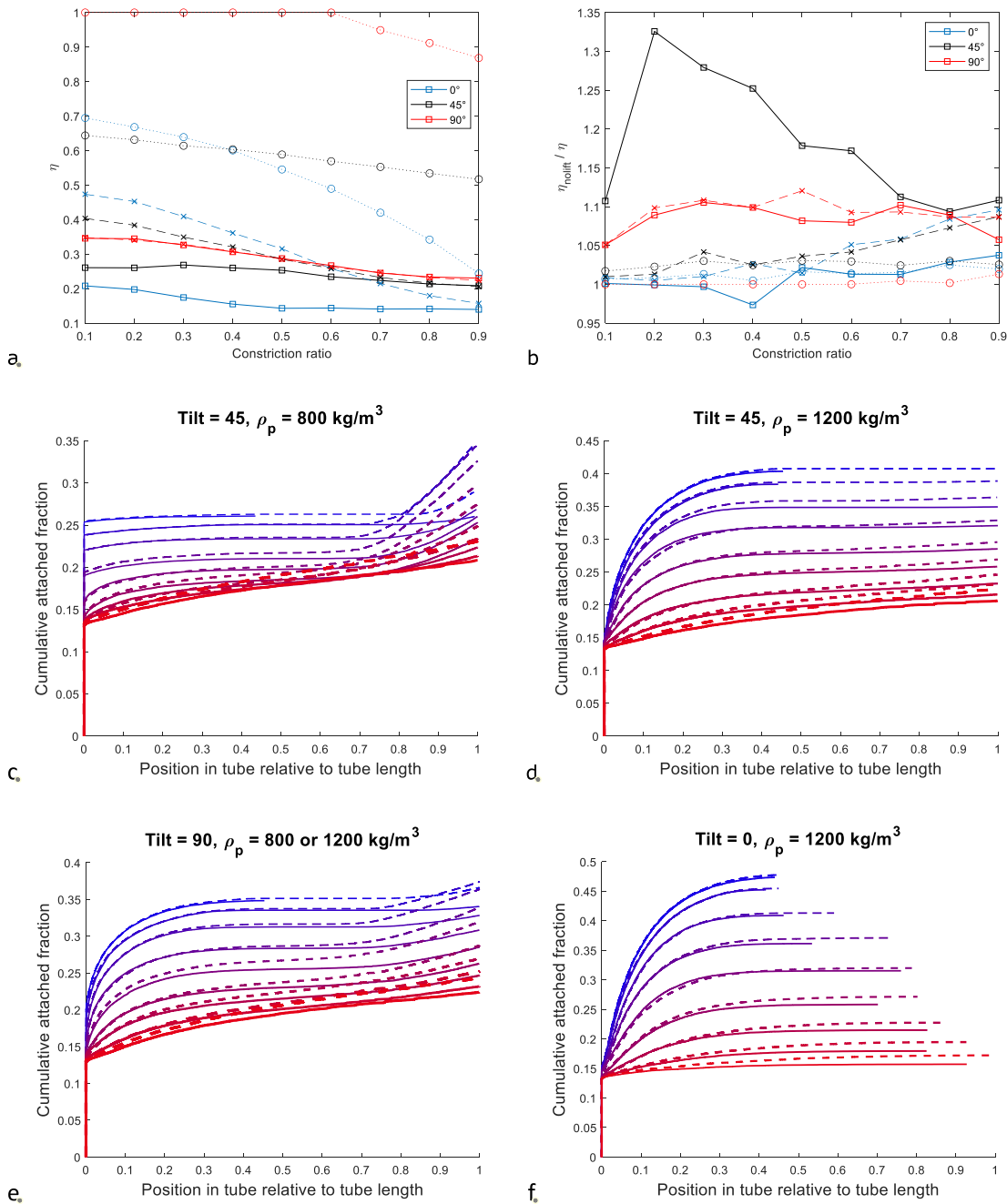
**Figure 6.** (a) Collection efficiencies of the additional simulations in Section 3.6. Square markers, crosses, and circles refer to scenarios with particle density $\rho_p = 800$, 1,200, and 5,260 kg/m³, respectively. (b) Ratio of collection efficiencies of simulations with hydrodynamic lift omitted, over the full simulations, for three tilt angles relative to the vertical in hyperbolic constricted tubes. Subfigures (c–f) show the deposition morphologies in diagonally tilted HCT in simulations with (solid lines) and without (dashed lines) hydrodynamic lift. Red lines represent scenarios with larger constriction ratios, and blue lines represent scenarios with smaller constriction ratios. Thicker lines represent scenarios with a larger fraction of deposited particles located in the middle portion of the constricted tube (relative position between 0.25 and 0.75).

torques immobilizing the colloid to the collector surface. This implies that regions of the pore space that colloids preferentially deposit are also least likely to experience hydrodynamically driven detachment. Of the three mechanisms, rolling requires the lowest fluid velocity to occur in most circumstances (Burdick et al., 2001). Rolling occurs when

$$M_d + F_x l_z > F_z l_x \tag{14}$$

where $M_d$ is the moment of surface stresses, $l_z$ is the rolling lever arm length, and $l_x$ is the adhesive lever arm length, given by

$$M_d = 8\pi\mu a^2 F_9 u_x \tag{15}$$

$$l_z = a + h_{\min} - h_{\text{asp}} \tag{16}$$

$$l_x = \sqrt{a^2 - l_z^2} \tag{17}$$

where $h_{\min} \approx 0.4 \, \text{nm}$ (Abdelfatah et al., 2017; Albojamal & Vafai, 2020) is the minimum separation distance between an attached particle and the collector surface, and $h_{\text{asp}}$ is the height of the surface asperity that the particle has to overcome by rolling (Burdick et al., 2005). Thus, the critical fluid velocity $u_{\text{crit}}$ that would detach attached particles is

$$8\pi\mu a^2 F_9 u_{\text{crit}} + \left[6\pi\mu a F_8 u_{\text{crit}} + F_{g,x}\right] l_z > \left[F_{\text{VDW}} + F_{g,z}\right] l_x \tag{18}$$

Since $a$ is micrometer-scale in this study, and by assuming $a \gg h_{asp} \gg h_{min}$, we approximate the lever arm lengths with $l_z \approx a$ and $l_x \approx \sqrt{2ah_{\text{asp}}}$, which yields a critical velocity of

$$u_{\text{crit}} \approx \frac{\left[F_{\text{VDW}} + F_{g,z}\right]\sqrt{2ah_{\text{asp}}} - F_{g,x}a}{\pi\mu a^2[8F_9 + 6F_8]} \tag{19}$$

At absolute separation distances of $h_{\min}$, the DLVO force is several orders of magnitude larger than the gravitational force acting on micrometer sized particles, so $F_g$ can be assumed negligible. Furthermore, since $a \gg h_{\min}$ the van der Waal's force may be simplified to

$$F_{\text{VDW}} \approx \frac{Aa}{6h_{\min}^2} \tag{20}$$

Substituting 20 into 19, and using $h_{\min} \approx 0.4 \, \text{nm}$, $u_{\text{crit}}$ may be further simplified to approximately

$$u_{\text{crit}} \approx \frac{A}{\pi\mu}\sqrt{\frac{h_{\text{asp}}}{a}} \cdot 10^{15} \, \text{m/s} \tag{21}$$

which clearly illustrates the dependence of $u_{\text{crit}}$ on $A$, $h_{\text{asp}}$, and $a$. For example, for an attached particle of radius $a \sim 1 \cdot 10^{-6} \, \text{m}$ with $A \sim 1 \cdot 10^{-20} \, \text{J}$, with an asperity of size $h_{\text{asp}} \approx 50 \, \text{nm}$, $u_{\text{crit}}$ would be around 20,000 mm/hr. Equation 21 implies that $u_{\text{crit}}$ is smaller for larger particles, due to its larger $M_d$ caused by the particle's larger surface area. In addition, the effective fluid velocity acting upon larger attached particles is larger due to their larger radii. Therefore, although the collection efficiency of larger particles tends to be larger, they are also more easily detached by hydrodynamic forces. Note that $u_{\text{crit}}$ depends on the square root of the dimensionless aspect ratio of asperity size over particle size. In contrast, $u_{\text{crit}}$ is directly proportional to $A$, implying that although the magnitude of the DLVO force has a relatively small effect on collection efficiencies, it is ultimately an important factor in transport and retention as it is the primary factor controlling the possibility of remobilization.

Figure 1b illustrates the fluid velocity in HCT constricted tube models, normalized against $u_m$. It shows that the fluid velocity maximizes at the constriction, and tapers off toward the axial extremities and pore walls. Therefore, if particles were to be hydrodynamically detached, most of it will occur for particles attached at or close to the tube constriction. Conversely, the deposition morphology of such particles, as previously discussed, is such that most particles entering the pore are deposited at the axial extremities of the pore, and few are deposited close to the constriction, for all three simulated orientations. Therefore, in constricted tube pore spaces, most attached particles are unlikely to be subsequently detached by hydrodynamic forces.

### 4.2. Environmental Consequences of Particle Deposition Morphology

The large pore-water velocities necessary for mechanical remobilization do not occur often under naturally occurring hydrological circumstances. In addition, in the unsaturated zone, soil water redistribution would also decrease the velocity of soil water. In settings where flow can be controlled, the fluid velocity may be increased to

facilitate hydrodynamic detachment of particles and reduce the favorability of particle attachment (Bedrikovetsky et al., 2012; Chang et al., 2008). For example, forced flow can successfully remediate clogged soil around wells (van Beek et al., 2009); fluid velocities around wells may reach up to 400 mm/hr (Chequer et al., 2021). However, this technique is effective only in the immediate vicinity of the well, as wells generate radial flow fields with geometrically decaying velocities (Tang & van der Zee, 2021). This difficulty in mechanical remobilization contributes to the effectiveness of soils and groundwater aquifers in filtering colloidal contaminants from marginal water under managed aquifer recharge (Sasidharan et al., 2021; Torkzaban et al., 2019; Wang et al., 2020), where organic contaminants may undergo in-situ biodegradation over time (Y. M. Chen et al., 1992).

Despite the difficulty of mechanical remobilization, detachment from DLVO potential minima may also transpire due to other processes. If attached particles form agglomerates with other particles, they experience larger detachment forces due to their increased size and an extended rolling lever arm length ($l_z$). The attachment of large agglomerates to pore walls results in increased fluid velocity within the tube, owing to a reduction in pore void volume. These factors collectively enhance the remobilization of agglomerates, either by detachment or disintegration (Kermani et al., 2020). Nanoscale surface roughness on pore walls can enhance the likelihood of particle detachment by weakening the potential minima of the DLVO interaction (Bergendahl & Grasso, 2000; Hoek & Agarwal, 2006). The presence of extended DLVO interactions (Abdelfatah et al., 2017), which typically yield shallower primary minima, may also facilitate detachment (VanNess et al., 2019). Chemical perturbations, such as decreasing the ionic strength of the pore water (Carstens et al., 2019), may weaken the attractive DLVO force (Liang et al., 2013), which we have shown is the strongest determining factor in the possibility of mechanical remobilization. Such chemical processes may thus aid or complement the mechanical remobilization of particles, and represent a promising area for future research; for example, a combination of chemical alteration and fluid flow may effectively remobilize attached particles (Zhuang et al., 2009).

## 5. Implications for Continuum-Scale Colloid Transport Modeling

The collection efficiency $\eta$ of individual pore throats, as determined through the methods introduced in this study, may be upscaled to determine the transport and breakthrough of colloids through a porous medium comprised of a continuum of pore throats. This may be done by defining a kinetic attachment coefficient, which is a function of the collection efficiency (Lin et al., 2022). Since the collection efficiency depends significantly on the fluid velocity, the kinetic attachment coefficients will vary nonlinearly with fluid velocity, in agreement with experimental findings (Bennacer et al., 2022; Zheng et al., 2014). The effects of deposition-unfavorable conditions, such as energy barriers, may be accounted for by multiplying the attachment coefficient with a sticking efficiency parameter. Therefore, obtaining the collection efficiency $\eta$, as we did in this study, is a crucial step in quantifying colloid attachment also in the presence of repulsive barriers. Recent research on cylindrical pore throats (Lin et al., 2021, 2022) has shown that not only is $\eta$ highly sensitive to fluid velocity, colloid size, and pore size, in agreement with our study, but so is the sticking efficiency for characterizing attachment through energy barriers. Since the fluid velocity and the ratio of colloid radius to pore radius changes drastically within a single constricted tube pore, and since pore shapes are heterogeneous in real soils, future research is necessary to elucidate the effects of pore throat geometry and orientation on the sticking efficiency. That would complement this study on the collection efficiency, and is necessary for comprehensively characterizing the transport of non-Brownian particles at a continuum scale.

Another implication for continuum-scale modeling is evident in Figure 4: the time at which non-attached particles exit the pore-space is smallest in scenarios with large $u_m$, due to fast advection, or large $S$, due to large gravitational acceleration. This means that even though the breakthrough fraction $(1 − \eta)$ is larger under small $S$, the breakthrough time is earlier under large $S$. Therefore, continuum models of particle transport that employ simple retardation or non-linear adsorption isotherms to characterize particle transport might not adequately physically characterize microparticle transport, even if observed breakthrough curves appear to empirically fit such models under certain parameterizations (e.g., Yoon et al., 2006). This is because continuum adsorption attachment models typically associate earlier breakthrough times with larger breakthrough fractions.

In summary, this study has contributed toward understanding how the collection efficiency and deposition morphology in various pore space geometries and orientations depend on the settling number S. S quantifies the relative dominance of gravitational over hydrodynamic drag forces, and depends on the physical properties of the colloid and fluid, and on fluid velocity. For the sake of comprehensiveness, we also considered other processes

(hydrodynamic lift, Brownian motion, and DLVO interactions), which results show generally have minor impacts but become more important in low-S scenarios. This understanding is crucial for predicting the fate of particulate environmental pollutants, and developing advanced continuum-scale models of colloid transport under environmental fluxes in real soils, where pore spaces are heterogeneous and advection paths are tortuous.

## 6. Conclusions

Colloid transport and fate under conditions with attractive DLVO potentials hinge heavily on the interplay between gravity and hydrodynamic drag. In all scenarios, which assume favorable conditions for attachment, the strength of the DLVO force had negligible effects on particle fate. The observed variability in collection efficiency in our simulations can be primarily ascribed to the dimensionless ratio S, defined as gravitational forces over average drag forces, and also to the tube geometry (for lighter particles, $S << 1$) or tube orientation (for denser particles, $S >> 1$). To a lesser yet possibly significant degree, depending on the magnitude of S, Brownian motion and the hydrodynamic lift force also contribute toward determining particle trajectories. These secondary factors are important in characterizing the transport of buoyant particles particularly when the mean direction of flow is opposite to gravitation, an example being downwards infiltration into soils. In such situations, the two strongest forces (gravity and hydrodynamic drag) act in opposite directions on average, thereby amplifying the overall influence of the secondary factors on particle trajectories.

Across all investigated scenarios, particles showed a preference for adhering to the axial extremities of constricted tubes, regardless of pore shape, tube orientation, particle size, or fluid velocity. Moreover, colloids attaching to the axial extremities of soil pore throats are less likely to be remobilized through mechanical detachment, particularly under natural hydrological flow rates. Crucially, regions of lower fluid velocities show a higher likelihood of particle attachment and a lower likelihood of remobilization. Consequently, the mechanical remobilization of particles is particularly challenging. Thus, remediation of soils and aquifers contaminated with microparticle pollutants may find more success with chemical or biological approaches than mechanical approaches. As we study various pore-space geometries, orientations, and sizes, this study on pore-scale colloid transport also has important implications for understanding and modeling continuum-scale transport in real soils with heterogeneous pore structures and tortuous flow paths.

## Appendix A: Coordinate and Vector Transformations

The three-dimensional pore-space is characterized by cylindrical coordinates $(r, s, \theta)$. Let the center of the particle's current position in the axisymmetric tube be $(r = r_p, s = s_p, \theta = \theta_p)$ in cylindrical coordinates. A local Cartesian coordinate system $(x, y, z)$ is used for the calculation of the force balance and particle-wall interactions, where the wall lies on the $(x, y)$ plane and the particle is located at $(0, 0, z_p)$.

Streamline vectors in the cylindrical coordinate system $(u_r, u_s)$ are converted to the local coordinate system $(u_x, u_z)$ with

$$u_x = -u_s \cos \alpha_{\text{slope}} - u_r \sin \alpha_{\text{slope}} \tag{A1}$$

$$u_z = u_s \sin \alpha_{\text{slope}} - u_r \cos \alpha_{\text{slope}} \tag{A2}$$

$$\alpha_{\text{slope}} = \tan^{-1}\left(\frac{dr_w}{ds}\right) \tag{A3}$$

where $\alpha_{\text{slope}}(s)$ is the local slope angle of the pore wall relative to the direction of mean flow, and $r_w(s)$ is the radius of the pore throat at $s$.

At the middle of a vertically oriented constricted tube, the pore wall is locally vertical; this is defined as a slope angle of $\alpha_{\text{slope}} = 0$. The gravitational force vector $\tilde{F}_{\text{grav}}$ acting on a particle located halfway through the depth of the tube, in terms of the local Cartesian coordinate system $(x, y, z)$, is therefore

$$\tilde{F}_{\text{grav}} = \frac{4}{3}\pi a^3 g(\rho_p - \rho_f) \begin{bmatrix} 1 \\ 0 \\ 0 \end{bmatrix} \tag{A4}$$

where $g$ is the gravitational constant. To account for the slope angle $\alpha_{\text{slope}}$ of the pore wall when the particle is at other locations within the pore, and to account for the tilting angle $\phi$ of the constricted tube relative to the vertical, we apply a tilting matrix $\boldsymbol{R}_t$ and a slope matrix $\boldsymbol{R}_s$ to the gravitational force vector

$$\boldsymbol{F}_{\text{grav}} = \boldsymbol{R}_s \boldsymbol{R}_t \tilde{\boldsymbol{F}}_{\text{grav}} \tag{A5}$$

$$\boldsymbol{R}_t = \begin{bmatrix} \cos(\phi) & -\sin(\theta)\sin(\phi) & -\cos(\theta)\sin(\phi) \\ \sin(\theta)\sin(\phi) & \cos(\phi) + \cos^2(\theta)[1-\cos^2(\phi)] & -\cos(\theta)\sin(\theta)[1-\cos^2(\phi)] \\ \cos(\theta)\sin(\phi) & -\cos(\theta)\sin(\theta)[1-\cos^2(\phi)] & \cos(\phi) + \sin^2(\theta)[1-\cos^2(\phi)] \end{bmatrix} \tag{A6}$$

$$\boldsymbol{R}_s = \begin{bmatrix} \cos(\alpha_{\text{slope}}) & 0 & \sin(\alpha_{\text{slope}}) \\ 0 & 0 & 0 \\ -\sin(\alpha_{\text{slope}}) & 0 & \cos(\alpha_{\text{slope}}) \end{bmatrix} \tag{A7}$$

Hence, the gravitational vector $\boldsymbol{g}$ in Equation 2 is

$$\boldsymbol{g} = \boldsymbol{R}_s \boldsymbol{R}_t \begin{bmatrix} g \\ 0 \\ 0 \end{bmatrix} \tag{A8}$$

After the force balance calculations, trajectory vectors in the local coordinate system $(dx, dy, dz)$ are converted to the original cylindrical coordinate system $(dr, ds, d\theta)$ through the following transformations:

$$dr = -dx \sin \alpha_{\text{slope}} - dz \cos \alpha_{\text{slope}} + \left[ \sqrt{(dy)^2 + r^2} - r \right] \tag{A9}$$

$$ds = -dx \cos \alpha_{\text{slope}} - dz \sin \alpha_{\text{slope}} \tag{A10}$$

$$d\theta = \operatorname{atan}\left(\frac{dy}{r}\right) \tag{A11}$$

The locations of the particles are then updated in the cylindrical coordinate system, so that the appropriate fluid velocities for the subsequent time step can be calculated.

## Data Availability Statement

Data were not used, nor created for this research.

## References

Abdelfatah, E., Kang, K., Pournik, M., Shiau, B. J. B., & Harwell, J. (2017). Mechanistic study of nanoparticles deposition and release in porous media. *Journal of Petroleum Science and Engineering*, *157*, 816–832. https://doi.org/10.1016/j.petrol.2017.08.003

Adamczyk, Z. (2017). *Particles at interfaces: Interactions, deposition, structure* (Vol. 20). Academic Press.

Adamczyk, Z., & Weroński, P. (1999). Application of the DLVO theory for particle deposition problems. *Advances in Colloid and Interface Science*, *83*(1–3), 137–226. https://doi.org/10.1016/s0001-8686(99)00009-3

Albojamal, A., & Vafai, K. (2020). Analysis of particle deposition of nanofluid flow through porous media. *International Journal of Heat and Mass Transfer*, *161*, 120227. https://doi.org/10.1016/j.ijheatmasstransfer.2020.120227

Auset, M., & Keller, A. A. (2006). Pore-scale visualization of colloid straining and filtration in saturated porous media using micromodels. *Water Resources Research*, *42*(12), W12S02. https://doi.org/10.1029/2005wr004639

Bear, J., & Cheng, A. H. D. (2010). *Modeling groundwater flow and contaminant transport* (Vol. 23). Springer Science & Business Media.

Bedrikovetsky, P., Siqueira, F. D., Furtado, C. A., & Souza, A. L. S. (2011). Modified particle detachment model for colloidal transport in porous media. *Transport in Porous Media*, *86*(2), 353–383. https://doi.org/10.1007/s11242-010-9626-4

Bedrikovetsky, P., Zeinijahromi, A., Siqueira, F. D., Furtado, C. A., & de Souza, A. L. S. (2012). Particle detachment under velocity alternation during suspension transport in porous media. *Transport in Porous Media*, *91*(1), 173–197. https://doi.org/10.1007/s11242-011-9839-1

Bennacer, L., Ahfir, N. D., Alem, A., & Huaqing, W. (2022). Influence of particles sizes and flow velocity on the transport of polydisperse fine particles in saturated porous media: Laboratory experiments. *Water, Air, & Soil Pollution*, *233*(7), 1–10.

Bergendahl, J., & Grasso, D. (2000). Prediction of colloid detachment in a model porous media: Hydrodynamics. *Chemical Engineering Science*, *55*(9), 1523–1532. https://doi.org/10.1016/s0009-2509(99)00422-4

Bradford, S. A., Bettahar, M., Simunek, J., & Van Genuchten, M. T. (2004). Straining and attachment of colloids in physically heterogeneous porous media. *Vadose Zone Journal*, *3*(2), 384–394. https://doi.org/10.2113/3.2.384

Bradford, S. A., Sasidharan, S., Kim, H., & Hwang, G. (2018). Comparison of types and amounts of nanoscale heterogeneity on bacteria retention. *Frontiers in Environmental Science*, *6*, 56. https://doi.org/10.3389/fenvs.2018.00056

Burdick, G. M., Berman, N. S., & Beaudoin, S. P. (2001). Describing hydrodynamic particle removal from surfaces using the particle Reynolds number. *Journal of Nanoparticle Research*, *3*(5), 453–465. https://doi.org/10.1023/a:1012593318108

Burdick, G. M., Berman, N. S., & Beaudoin, S. P. (2005). Hydrodynamic particle removal from surfaces. *Thin Solid Films*, *488*(1), 116–123. https://doi.org/10.1016/j.tsf.2005.04.112

Carstens, J. F., Bachmann, J., & Neuweiler, I. (2019). A new approach to determine the relative importance of DLVO and non-DLVO colloid retention mechanisms in porous media. *Colloids and Surfaces A: Physicochemical and Engineering Aspects*, *560*, 330–335. https://doi.org/10.1016/j.colsurfa.2018.10.013

Chan, S. K., & Ng, K. M. (1988). Geometrical characteristics of the pore space in a random packing of equal spheres. *Powder Technology*, *54*(2), 147–155. https://doi.org/10.1016/0032-5910(88)80072-x

Chang, Y. I., Chen, S. C., & Lee, E. (2003). Prediction of Brownian particle deposition in porous media using the constricted tube model. *Journal of Colloid and Interface Science*, *266*(1), 48–59. https://doi.org/10.1016/s0021-9797(03)00636-2

Chang, Y. I., Huang, Y. T., Luo, Z. L., & Zhang, G. Z. (2008). A study on particle deposition morphology within a constricted tube in the presence and absence of the detachment mechanism. *Separation and Purification Technology*, *63*(3), 566–576. https://doi.org/10.1016/j.seppur.2008.06.022

Chaumeil, F., & Crapper, M. (2014). Using the DEM-CFD method to predict Brownian particle deposition in a constricted tube. *Particuology*, *15*, 94–106. https://doi.org/10.1016/j.partic.2013.05.005

Chen, G., Hong, Y., & Walker, S. L. (2010). Colloidal and bacterial deposition: Role of gravity. *Langmuir*, *26*(1), 314–319. https://doi.org/10.1021/la903089x

Chen, L., Li, D., Ming, F., Shi, X., & Chen, X. (2019). A fractal model of hydraulic conductivity for saturated frozen soil. *Water*, *11*(2), 369. https://doi.org/10.3390/w11020369

Chen, Y. M., Abriola, L. M., Alvarez, P. J., Anid, P. J., & Vogel, T. M. (1992). Modeling transport and biodegradation of benzene and toluene in sandy aquifer material: Comparisons with experimental measurements. *Water Resources Research*, *28*(7), 1833–1847. https://doi.org/10.1029/92wr00667

Chequer, L., Nguyen, C., Loi, G., Zeinijahromi, A., & Bedrikovetsky, P. (2021). Fines migration in aquifers: Production history treatment and well behaviour prediction. *Journal of Hydrology*, *602*, 126660. https://doi.org/10.1016/j.jhydrol.2021.126660

Chrysikopoulos, C. V., & Syngouna, V. I. (2014). Effect of gravity on colloid transport through water-saturated columns packed with glass beads: Modeling and experiments. *Environmental Science & Technology*, *48*(12), 6805–6813. https://doi.org/10.1021/es501295n

De Corato, M., Greco, F., D'Avino, G., & Maffettone, P. L. (2015). Hydrodynamics and Brownian motions of a spheroid near a rigid wall. *The Journal of Chemical Physics*, *142*(19), 194901. https://doi.org/10.1063/1.4920981

Di Carlo, D., Irimia, D., Tompkins, R. G., & Toner, M. (2007). Continuous inertial focusing, ordering, and separation of particles in microchannels. *Proceedings of the National Academy of Sciences of the United States of America*, *104*(48), 18892–18897. https://doi.org/10.1073/pnas.0704958104

Elimelech, M. (1994). Particle deposition on ideal collectors from dilute flowing suspensions: Mathematical formulation, numerical solution, and simulations. *Separations Technology*, *4*(4), 186–212. https://doi.org/10.1016/0956-9618(94)80024-3

Faure, B., Salazar-Alvarez, G., & Bergstrom, L. (2011). Hamaker constants of iron oxide nanoparticles. *Langmuir*, *27*(14), 8659–8664. https://doi.org/10.1021/la201387d

Felderhof, B. U., & Sellier, A. (2012). Mobility matrix of a spherical particle translating and rotating in a viscous fluid confined in a spherical cell, and the rate of escape from the cell. *The Journal of Chemical Physics*, *136*(5), 054703. https://doi.org/10.1063/1.3681368

Gupta, D., & Peters, M. H. (1985). A Brownian dynamics simulation of aerosol deposition onto spherical collectors. *Journal of Colloid and Interface Science*, *104*(2), 375–389. https://doi.org/10.1016/0021-9797(85)90046-3

Hoek, E. M., & Agarwal, G. K. (2006). Extended DLVO interactions between spherical particles and rough surfaces. *Journal of Colloid and Interface Science*, *298*(1), 50–58. https://doi.org/10.1016/j.jcis.2005.12.031

Johnson, W. P. (2020). Quantitative linking of nanoscale interactions to continuum-scale nanoparticle and microplastic transport in environmental granular media. *Environmental Science & Technology*, *54*(13), 8032–8042. https://doi.org/10.1021/acs.est.0c01172

Johnson, W. P., Li, X., & Assemi, S. (2007). Deposition and re-entrainment dynamics of microbes and non-biological colloids during non-perturbed transport in porous media in the presence of an energy barrier to deposition. *Advances in Water Resources*, *30*(6–7), 1432–1454. https://doi.org/10.1016/j.advwatres.2006.05.020

Johnson, W. P., Li, X., & Yal, G. (2007). Colloid retention in porous media: Mechanistic confirmation of wedging and retention in zones of flow stagnation. *Environmental Science & Technology*, *41*(4), 1279–1287. https://doi.org/10.1021/es061301x

Kermani, M. S., Jafari, S., Rahnama, M., & Raoof, A. (2020). Direct pore scale numerical simulation of colloid transport and retention. Part I: Fluid flow velocity, colloid size, and pore structure effects. *Advances in Water Resources*, *144*, 103694. https://doi.org/10.1016/j.advwatres.2020.103694

Khan, F. R., Syberg, K., & Palmqvist, A. (2017). Are standardized test guidelines adequate for assessing waterborne particulate contaminants?

Kooi, M., & Koelmans, A. A. (2019). Simplifying microplastic via continuous probability distributions for size, shape, and density. *Environmental Science and Technology Letters*, *6*(9), 551–557. https://doi.org/10.1021/acs.estlett.9b00379

Leij, F. J., Bradford, S. A., & Sciortino, A. (2016). Analytic solutions for colloid transport with time-and depth-dependent retention in porous media. *Journal of Contaminant Hydrology*, *195*, 40–51. https://doi.org/10.1016/j.jconhyd.2016.10.006

Li, X., Zhang, P., Lin, C. L., & Johnson, W. P. (2005). Role of hydrodynamic drag on microsphere deposition and re-entrainment in porous media under unfavorable conditions. *Environmental Science & Technology*, *39*(11), 4012–4020. https://doi.org/10.1021/es048814t

Liang, Y., Bradford, S. A., Simunek, J., Heggen, M., Vereecken, H., & Klumpp, E. (2013). Retention and remobilization of stabilized silver nanoparticles in an undisturbed loamy sand soil. *Environmental Science & Technology*, *47*(21), 12229–12237. https://doi.org/10.1021/es402046u

Lin, D., Hu, L., Bradford, S. A., Zhang, X., & Lo, I. M. (2021). Simulation of colloid transport and retention using a pore-network model with roughness and chemical heterogeneity on pore surfaces. *Water Resources Research*, *57*(2), e2020WR028571. https://doi.org/10.1029/2020wr028571

Lin, D., Zhang, X., Hu, L., Bradford, S. A., & Shen, C. (2022). Prediction of colloid sticking efficiency at pore-scale and macroscale using a pore network model. *Journal of Hydrology*, *612*, 128253. https://doi.org/10.1016/j.jhydrol.2022.128253

Ma, H., Hradisky, M., & Johnson, W. P. (2013). Extending applicability of correlation equations to predict colloidal retention in porous media at low fluid velocity. *Environmental Science & Technology*, *47*(5), 2272–2278. https://doi.org/10.1021/es304753r

Ma, H., Pazmino, E. F., & Johnson, W. P. (2011). Gravitational settling effects on unit cell predictions of colloidal retention in porous media in the absence of energy barriers. *Environmental Science & Technology*, *45*(19), 8306–8312. https://doi.org/10.1021/es200696x

Ma, H., Pedel, J., Fife, P., & Johnson, W. P. (2009). Hemispheres-in-cell geometry to predict colloid deposition in porous media. *Environmental Science & Technology*, *43*(22), 8573–8579. https://doi.org/10.1021/es901242b

Mackie, R. I., Horne, R. M. W., & Jarvis, R. J. (1987). Dynamic modeling of deep-bed filtration. *AIChE Journal*, *33*(11), 1761–1775. https://doi.org/10.1002/aic.690331102

Mahdavimanesh, M., Noghrehabadi, A. R., Behbahaninejad, M., Ahmadi, G., & Dehghanian, M. (2013). Lagrangian particle tracking: Model development. *Life Science Journal*, *10*(8s), 34–41.

McGechan, M. B., & Lewis, D. R. (2002). SW—Soil and water: Transport of particulate and colloid-sorbed contaminants through soil, part 1: General principles. *Biosystems Engineering*, *83*(3), 255–273. https://doi.org/10.1006/bioe.2002.0125

Messina, F., Marchisio, D. L., & Sethi, R. (2015). An extended and total flux normalized correlation equation for predicting single-collector efficiency. *Journal of Colloid and Interface Science*, *446*, 185–193. https://doi.org/10.1016/j.jcis.2015.01.024

Molnar, I. L., Johnson, W. P., Gerhard, J. I., Willson, C. S., & O'Carroll, D. M. (2015). Predicting colloid transport through saturated porous media: A critical review. *Water Resources Research*, *51*(9), 6804–6845. https://doi.org/10.1002/2015wr017318

Nelson, K. E., & Ginn, T. R. (2005). Colloid filtration theory and the Happel sphere-in-cell model revisited with direct numerical simulation of colloids. *Langmuir*, *21*(6), 2173–2184. https://doi.org/10.1021/la048404i

Nizzetto, L., Bussi, G., Futter, M. N., Butterfield, D., & Whitehead, P. G. (2016). A theoretical assessment of microplastic transport in river catchments and their retention by soils and river sediments. *Environmental Sciences: Processes & Impacts*, *18*(8), 1050–1059. https://doi.org/10.1039/c6em00206d

Payatakes, A. C., Tien, C., & Turian, R. M. (1973a). A new model for granular porous media: Part I. Model formulation. *AIChE Journal*, *19*(1), 58–67. https://doi.org/10.1002/aic.690190110

Payatakes, A. C., Tien, C., & Turian, R. M. (1973b). A new model for granular porous media: Part II. Numerical solution of steady state incompressible Newtonian flow through periodically constricted tubes. *AIChE Journal*, *19*(1), 67–76. https://doi.org/10.1002/aic.690190111

Pazmino, E., Trauscht, J., Dame, B., & Johnson, W. P. (2014). Power law size-distributed heterogeneity explains colloid retention on soda lime glass in the presence of energy barriers. *Langmuir*, *30*(19), 5412–5421. https://doi.org/10.1021/la501006p

Pazmino, E., Trauscht, J., & Johnson, W. P. (2014). Release of colloids from primary minimum contact under unfavorable conditions by perturbations in ionic strength and flow rate. *Environmental Science & Technology*, *48*(16), 9227–9235. https://doi.org/10.1021/es502503y

Rafique, A., Irfan, M., Mumtaz, M., & Qadir, A. (2020). Spatial distribution of microplastics in soil with context to human activities: A case study from the urban center. *Environmental Monitoring and Assessment*, *192*(11), 1–13. https://doi.org/10.1007/s10661-020-08641-3

Rasmuson, A., Erickson, B., Borchardt, M., Muldoon, M., & Johnson, W. P. (2019). Pathogen prevalence in fractured versus granular aquifers and the role of forward flow stagnation zones on pore-scale delivery to surfaces. *Environmental Science & Technology*, *54*(1), 137–145. https://doi.org/10.1021/acs.est.9b03274

Rasmuson, A., VanNess, K., Ron, C. A., & Johnson, W. P. (2019). Hydrodynamic versus surface interaction impacts of roughness in closing the gap between favorable and unfavorable colloid transport conditions. *Environmental Science & Technology*, *53*(5), 2450–2459. https://doi.org/10.1021/acs.est.8b06162

Saffman, P. G. T. (1965). The lift on a small sphere in a slow shear flow. *Journal of Fluid Mechanics*, *22*(2), 385–400. https://doi.org/10.1017/s0022112065000824

Sasidharan, S., Bradford, S. A., Šimůnek, J., & Kraemer, S. R. (2021). Virus transport from drywells under constant head conditions: A modeling study. *Water Research*, *197*, 117040. https://doi.org/10.1016/j.watres.2021.117040

Schmitz, R. M. (2006). Can the diffuse double layer theory describe changes in hydraulic conductivity of compacted clays? *Geotechnical & Geological Engineering*, *24*(6), 1835–1844. https://doi.org/10.1007/s10706-005-3365-2

Seetha, N., Kumar, M. M., Hassanizadeh, S. M., & Raoof, A. (2014). Virus-sized colloid transport in a single pore: Model development and sensitivity analysis. *Journal of Contaminant Hydrology*, *164*, 163–180. https://doi.org/10.1016/j.jconhyd.2014.05.010

Shen, C., Bradford, S. A., Li, T., Li, B., & Huang, Y. (2018). Can nanoscale surface charge heterogeneity really explain colloid detachment from primary minima upon reduction of solution ionic strength? *Journal of Nanoparticle Research*, *20*(6), 1–18. https://doi.org/10.1007/s11051-018-4265-8

Spielman, L. A., & Fitzpatrick, J. A. (1973). Theory for particle collection under London and gravity forces. *Journal of Colloid and Interface Science*, *42*(3), 607–623. https://doi.org/10.1016/0021-9797(73)90047-7

Tang, D. W. S., & van der Zee, S. E. A. T. M. (2021). Dispersion and recovery of solutes and heat under cyclic radial advection. *Journal of Hydrology*, *602*, 126713. https://doi.org/10.1016/j.jhydrol.2021.126713

Tang, D. W. S., & Van Der Zee, S. E. A. T. M. (2022). Macrodispersion and recovery of solutes and heat in heterogeneous aquifers. *Water Resources Research*, *58*(2), e2021WR030920. https://doi.org/10.1029/2021wr030920

Torkzaban, S., Hocking, M., Bradford, S. A., Tazehkand, S. S., Sasidharan, S., & Šimůnek, J. (2019). Modeling virus transport and removal during storage and recovery in heterogeneous aquifers. *Journal of Hydrology*, *578*, 124082. https://doi.org/10.1016/j.jhydrol.2019.124082

Vaidyanathan, R., & Tien, C. (1988). Hydrosol deposition in granular beds. *Chemical Engineering Science*, *43*(2), 289–302. https://doi.org/10.1016/0009-2509(88)85041-3

Van Beek, C. G. E. M., Breedveld, R. J. M., Juhász-Holterman, M., Oosterhof, A., & Stuyfzand, P. J. (2009). Cause and prevention of well bore clogging by particles. *Hydrogeology Journal*, *17*(8), 1877–1886. https://doi.org/10.1007/s10040-009-0537-9

VanNess, K., Rasmuson, A., Ron, C. A., & Johnson, W. P. (2019). A unified force and torque balance for colloid transport: Predicting attachment and mobilization under favorable and unfavorable conditions. *Langmuir*, *35*(27), 9061–9070. https://doi.org/10.1021/acs.langmuir.9b00911

Wang, C., Wang, R., Huo, Z., Xie, E., & Dahlke, H. E. (2020). Colloid transport through soil and other porous media under transient flow conditions—A review. *Wiley Interdisciplinary Reviews: Water*, *7*(4), e1439. https://doi.org/10.1002/wat2.1439

Warszyński, P. (2000). Coupling of hydrodynamic and electric interactions in adsorption of colloidal particles. *Advances in Colloid and Interface Science*, *84*(1–3), 47–142. https://doi.org/10.1016/s0001-8686(99)00015-9

Williamson, K. E., Fuhrmann, J. J., Wommack, K. E., & Radosevich, M. (2017). Viruses in soil ecosystems: An unknown quantity within an unexplored territory. *Annual review of virology*, *4*(1), 201–219. https://doi.org/10.1146/annurev-virology-101416-041639

Yang, B. H., Wang, J., Joseph, D. D., Hu, H. H., Pan, T. W., & Glowinski, R. (2005). Migration of a sphere in tube flow. *Journal of Fluid Mechanics*, *540*, 109–131. https://doi.org/10.1017/s0022112005005677

Yang, Y., Rutland, C., & Rothamer, D. (2018). Study of the deep-bed filtration using pore filtration model (PFM). *SAE International Journal of Fuels and Lubricants*, *11*(4), 287–300. https://doi.org/10.4271/2018-01-0956

Yao, K. M., Habibian, M. T., & O'Melia, C. R. (1971). Water and waste water filtration. Concepts and applications. *Environmental Science & Technology*, *5*(11), 1105–1112. https://doi.org/10.1021/es60058a005

Yoon, J. S., Germaine, J. T., & Culligan, P. J. (2006). Visualization of particle behavior within a porous medium: Mechanisms for particle filtration and retardation during downward transport. *Water Resources Research*, *42*(6), W06417. https://doi.org/10.1029/2004wr003660

Yu, C., Duan, P., Barry, D. A., Johnson, W. P., Chen, L., Yu, Z., et al. (2022). Colloidal transport and deposition through dense vegetation. *Chemosphere*, *287*, 132197. https://doi.org/10.1016/j.chemosphere.2021.132197

Zheng, X. L., Shan, B. B., Chen, L., Sun, Y. W., & Zhang, S. H. (2014). Attachment–detachment dynamics of suspended particle in porous media: Experiment and modeling. *Journal of Hydrology*, *511*, 199–204. https://doi.org/10.1016/j.jhydrol.2014.01.039

Zhuang, J., Tyner, J. S., & Perfect, E. (2009). Colloid transport and remobilization in porous media during infiltration and drainage. *Journal of Hydrology*, *377*(1–2), 112–119. https://doi.org/10.1016/j.jhydrol.2009.08.011